Electronic Supplementary Information

Amorphous NiFe Oxide Derived from Air-Pyrolyzed Prussian Blue Analogue with Rapid Complete Reconstruction for Enhanced Oxygen Evolution Reaction

Zhen Cao, Wenhui Yan, Haozhe Shi, Tingting Zhou,* Zhifei Sun, Yuhan Yang, Wenbin Zhang, Jiali Zhang and Kaili Wang *

College of Chemical Engineering and Environmental Chemistry, Weifang University, Weifang 261061, China

* Correspondence: zhoutt@wfu.edu.cn, 20220043@wfu.edu.cn

Experimental section

Materials. Nickel(II) dichloride ($CoCl_2 \cdot 6H_2O$, AR), potassium ferricyanide(III) ($K_3Fe(CN)_6$, AR), potassium hydroxide (KOH, AR), sodium citrate ($Na_3C_6H_5O_7 \cdot 2H_2O$, AR), and ethanol ($CH_3CH_2OH$, AR) were purchased from Sinopharm Chemical Reagent Co., Ltd. All chemicals were used as received without further purification. ULUPURE water (resistivity > 18 MΩ cm) was used throughout the experiments.

Synthesis of NiFe-PBA precursors and NiFe-PBA-Derived Catalysts. NiFe-PBA precursors were synthesized via a simple chemical precipitation method. Briefly, 6.75 mmol sodium citrate was dissolved in 150 mL H_2O; then 4.5 mmol $NiCl_2$ was added into the above solution. Next, 3mmol $K_3Fe(CN)_6$ was dissolved in 150 mL H_2O. These two solutions were mixed and magnetic stirred for 5 min. Then obtained mixed solution was aged for 7 days at room temperature and washed several times with absolute ethanol and dried at 80 ^oC overnight in vacuum.

The as-prepared NiFe-PBA precursors were calcined in a tube furnace with the following protocol: heating in air to target temperatures (200, 250, 300, and 350 °C) with a ramp rate of 2 °C min^{-1}, with a 2-hour hold at temperature, and subsequent furnace cooling.

Characterization. Powder X-ray diffraction (XRD) data were collected using a SmartLab 9kw diffractometer equipped with Cu Kα radiation. Scanning electron microscopy (SEM) images were performed using a ZEISS MERLIN. X-ray photoelectron spectroscopy (XPS) measurements were performed on a ThermoFisher ESCALAB 250Xi. Transmission electron microscopy (TEM) and high-resolution transmission electron microscopy (HRTEM) images were obtained with a JEOL JEM-2100 at 200 kV. Fourier transform infrared (FT-IR) spectroscopys were performed on FTIR-850 spectrometer of SCI.&TECH. CO,. LTD. Thermal gravimetric (TG) analysis was performed to investigate the stability of NiFe-PBA by TGA instrument model HENVEN HCT-4, under a flow of air. Raman spectra were recorded on a Horiba LabRAM HR Evolution Raman microscope with a 532 nm excitation laser. Electron Spin Resonance (ESR) measurements were performed using a Bruker EMXplus-6/1 spectrometer. Inductively coupled plasma optical emission spectrometry (ICP-OES) analysis was conducted using an EXPEC 6000 spectrometer.

Electrochemical Measurements. A typical three-electrode system was used on a CHI 760E electrochemical workstation to test the electrochemical performance in an electrolyte of 1 M KOH. The working electrode, reference electrode, and counter electrode were a glassy carbon (GC) electrode (5 mm in diameter) loaded with the electrocatalyst, a Hg/HgO (1 M KOH) electrode, and a platinum plate, respectively. To prepare the working electrodes, 6 mg of the as-prepared catalyst and 2 mg of carbon black (Vulcan XC-72) were dispersed in a mixture of 720 μL of ethanol, 700 μL of water, and 80 μL of Nafion solution (5 wt%). The mixture was then sonicated for 30 minutes to form a homogeneous ink. Subsequently, 10 μL of the catalyst ink was drop-cast onto the GC electrode and dried. All polarization measurements were performed at a scan rate of 5 mV s^{-1}. The measured potentials were converted to the reversible hydrogen electrode (RHE) scale using the equation: E (vs. RHE) = E (vs. Hg/HgO) + 0.098 V + 0.0591×pH. All cyclic voltammetry (CV) and linear sweep voltammetry (LSV) tests on the rotating disk electrode (RDE) were performed with 90% iR compensation. Ni foam (NF)-supported electrodes were prepared as follows: For coated electrodes, the catalyst ink was applied onto pre-cleaned nickel foam pieces (1 cm × 1 cm) and dried at 60 °C for 1 hour. Electrodes that were directly grown on NF were simply cut into 1 cm × 1 cm pieces and used without further processing.

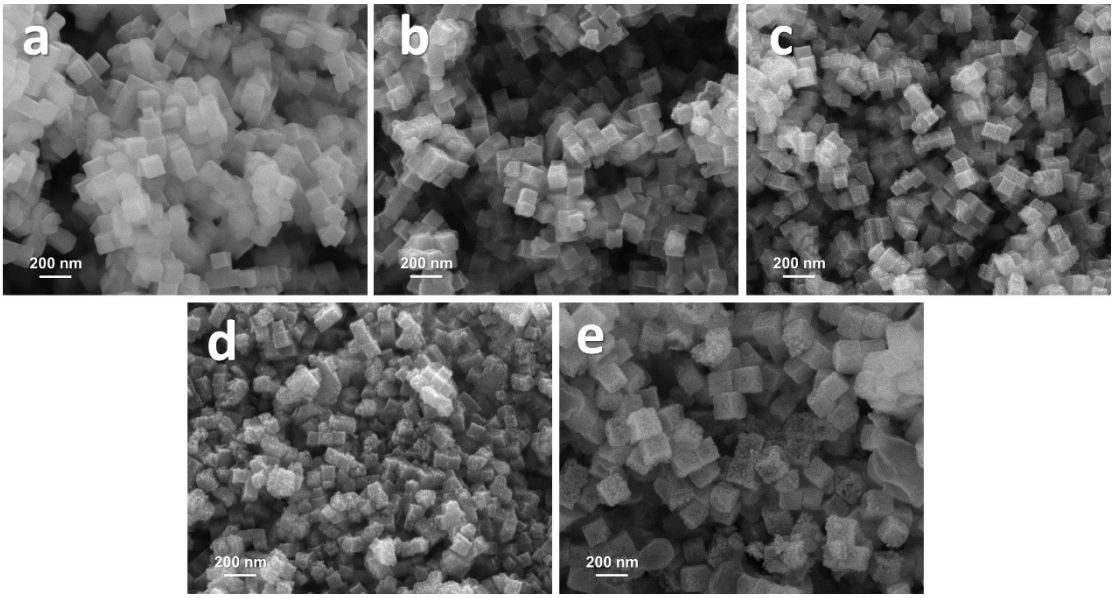

Figure S1. The SEM images of (a) NiFe-PBA, (b) NiFe-200, (c) NiFe-250, (d) NiF3-300 and (e) NiFe-350.

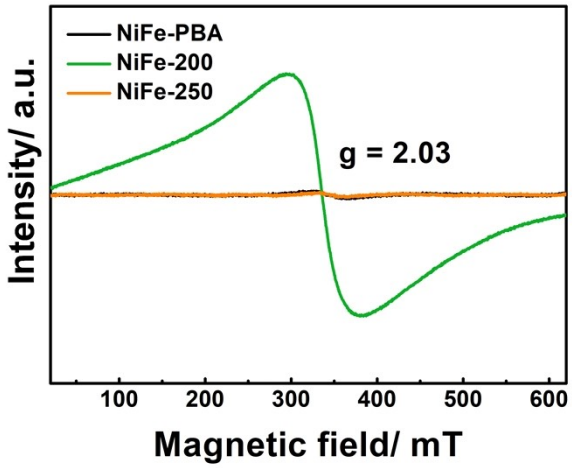

Figure S2. ESR spectra of NiFe-PBA, NiFe-200 and NiFe-250.

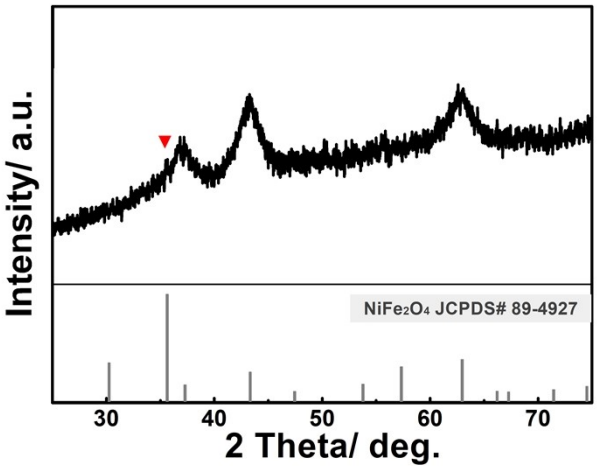

Figure S3. XRD pattern of NiFe-PBA heated in air at 400 °C.

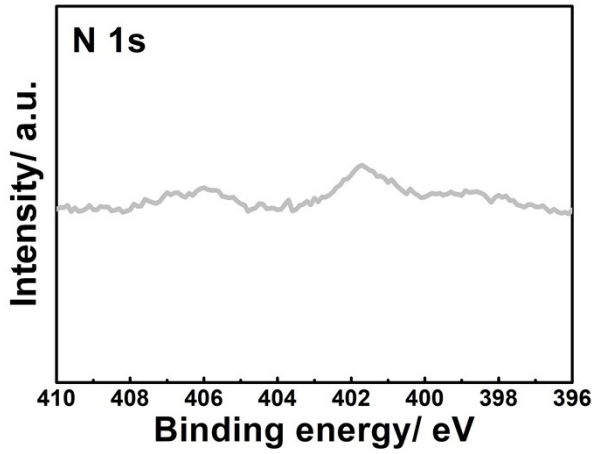

Figure S4. High-resolution XPS spectrum of Ni 1s of NiFe-250.

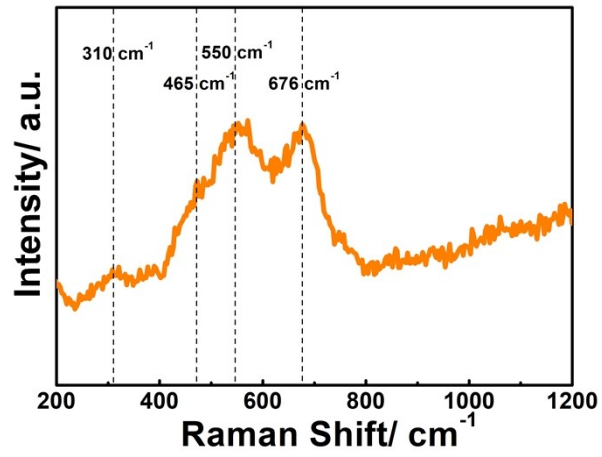

Figure S5. Raman spectra of NiFe-250.

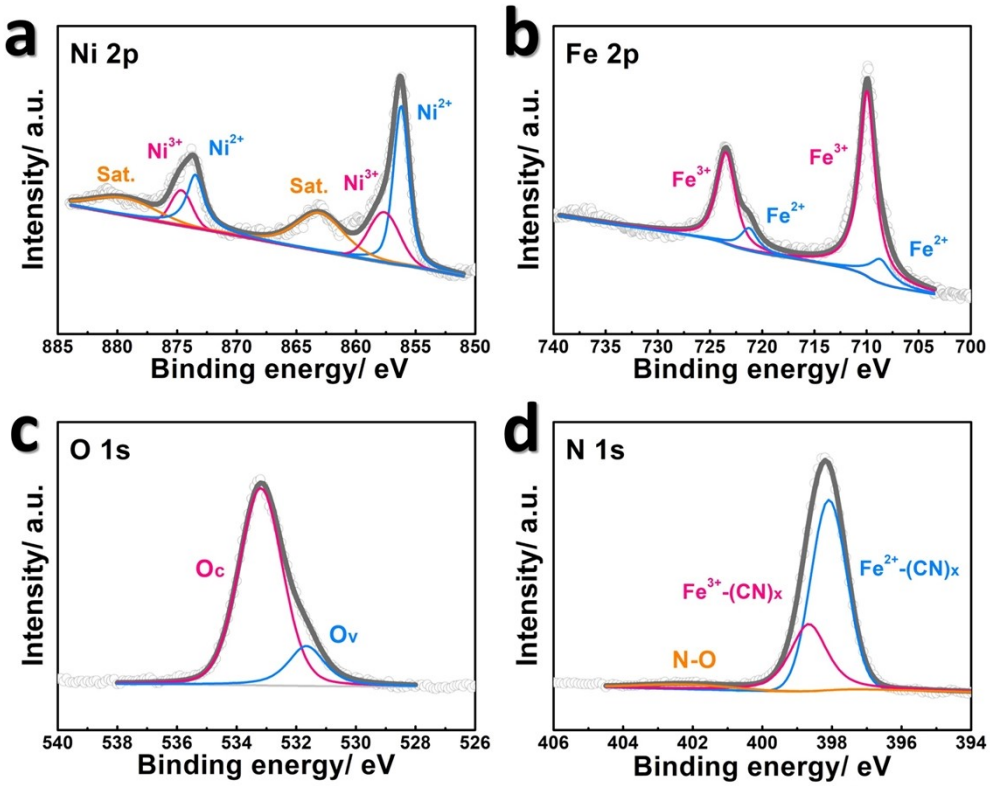

Figure S6. High-resolution XPS spectrum of NiFe-PBA : (a) Ni 2p, (b) Fe 2p, (c) O 1s and (d) N 1s.

The splitting peak of 856.21 and 873.58 eV should be attributed to Ni^{2+} in $Ni_3(Fe(CN)_6)_2 \cdot 10H_2O$ and peaks at 857.78 and 874.77 eV should be attributed to Ni^{3+} in $Ni_3(Fe(CN)_6)_2 \cdot 10H_2O$, respectively.[1, 2] The other peaks correspond to the satellite peaks of Ni. The peaks at 708.6 and 721.3 eV are attributed to Fe^{2+} in $Ni_3(Fe(CN)_6)_2 \cdot 10H_2O$ and peaks at 710.0 and 723.5 eV are attributed to Fe^{3+} in $Ni_3(Fe(CN)_6)_2 \cdot 10H_2O$, respectively. It is worth noting that no satellite peaks were observed at 732 and 719 eV in the spectrum of Fe 2p, indicating the absence of iron oxides.[1, 2] The peaks at 531.7 and 533.2 eV are attributed to O_v and O_c, respectively.[1] The peaks at 398.1 and 398.7 eV are attributed to Fe^{2+}-$(CN)_x$ and Fe^{3+}-$(CN)_x$, respectively. In addition, there are also small N-O signals that can be detected.[2, 3]

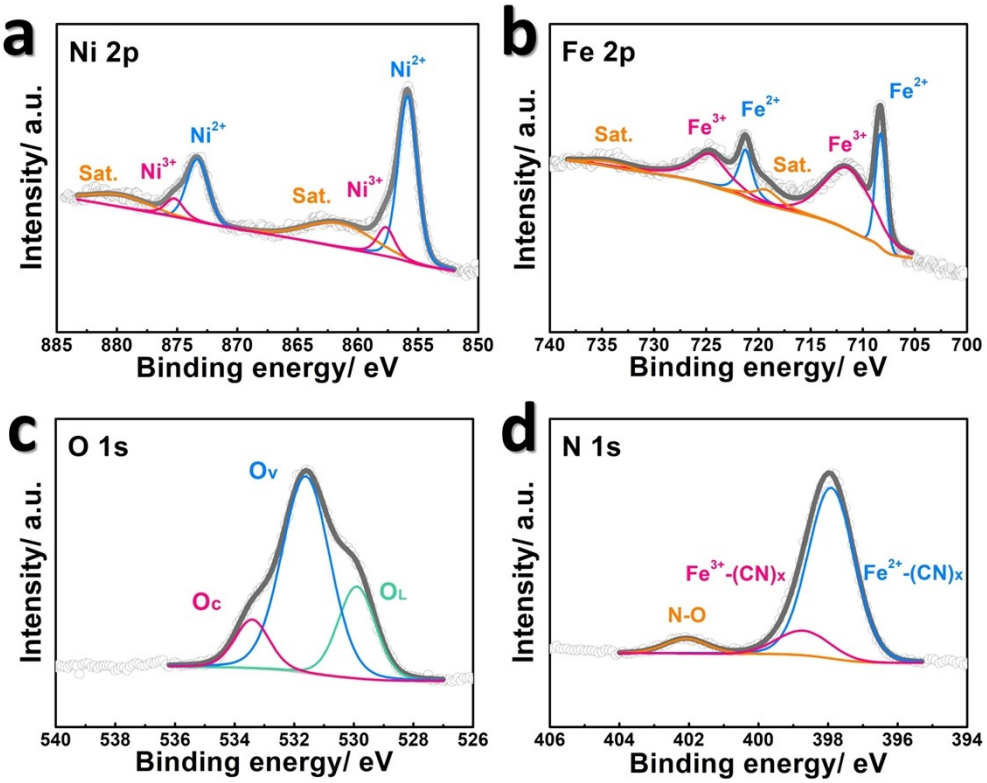

Figure S7. High-resolution XPS spectrum of NiFe-200 : (a) Ni 2p, (b) Fe 2p, (c) O 1s and (d) N 1s.

The splitting peak of 855.9 and 873.3 eV should be attributed to Ni^{2+} in $Ni_3(Fe(CN)_6)_2 \cdot 10H_2O$ and peaks at 857.6 and 875.2 eV should be attributed to Ni^{3+} in $Ni_3(Fe(CN)_6)_2 \cdot 10H_2O$, respectively. [1, 2] The other peaks correspond to the satellite peaks of Ni. The peaks at 708.4 and 721.5 eV are attributed to Fe^{2+} in $Ni_3(Fe(CN)_6)_2$ and peaks at 711.4 and 724.6 eV are attributed to Fe^{3+} in $Ni_3(Fe(CN)_6)_2 \cdot 10H_2O$, respectively. The other peaks correspond to the satellite peaks of Fe perhaps trace amounts of imperceptible oxides have already been produced at this time.[1, 2] The peaks at 529.9 531.6 and 533.3 eV are attributed to O_L, O_v and O_c, respectively.[1] The peaks at 398.1 and 398.7 eV are attributed to Fe^{2+}-$(CN)_x$ and Fe^{3+}-$(CN)_x$, respectively. In addition, there are also N-O signals that can be detected. From the figure, it can be inferred that after heat treatment at 200 ℃, some CN begins to precipitate and oxidize, with some O entering the PBA structure.[2, 3]

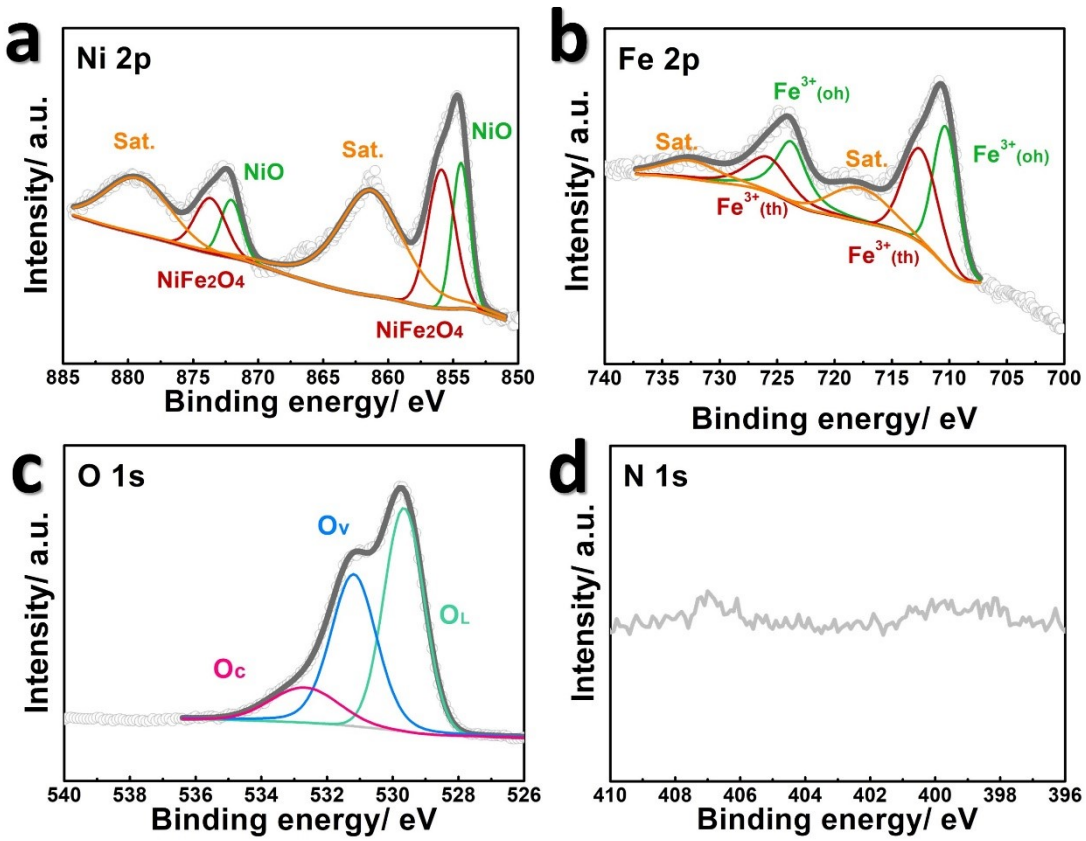

Figure S8. High-resolution XPS spectrum of NiFe-300 : (a) Ni 2p, (b) Fe 2p, (c) O 1s and (d) N 1s.

The splitting peak of 854.4 and 872.6 eV should be attributed to Ni^{2+} in NiO and peaks at 855.9 and 873.7 eV should be attributed to $NiFe_2O_4$, respectively. The other peaks correspond to the satellite peaks of Ni.[4, 5] The peaks at 710.3 and 723.8 eV are attributed to Fe^{3+}(oh) and peaks at 712.5 and 725.8 eV are attributed to Fe^{3+} (th), respectively. The other peaks correspond to the satellite peaks of Fe.[5] The peaks at 529.7, 531.3 and 533.2 eV are attributed to O_L, O_v and O_c, respectively.[6]

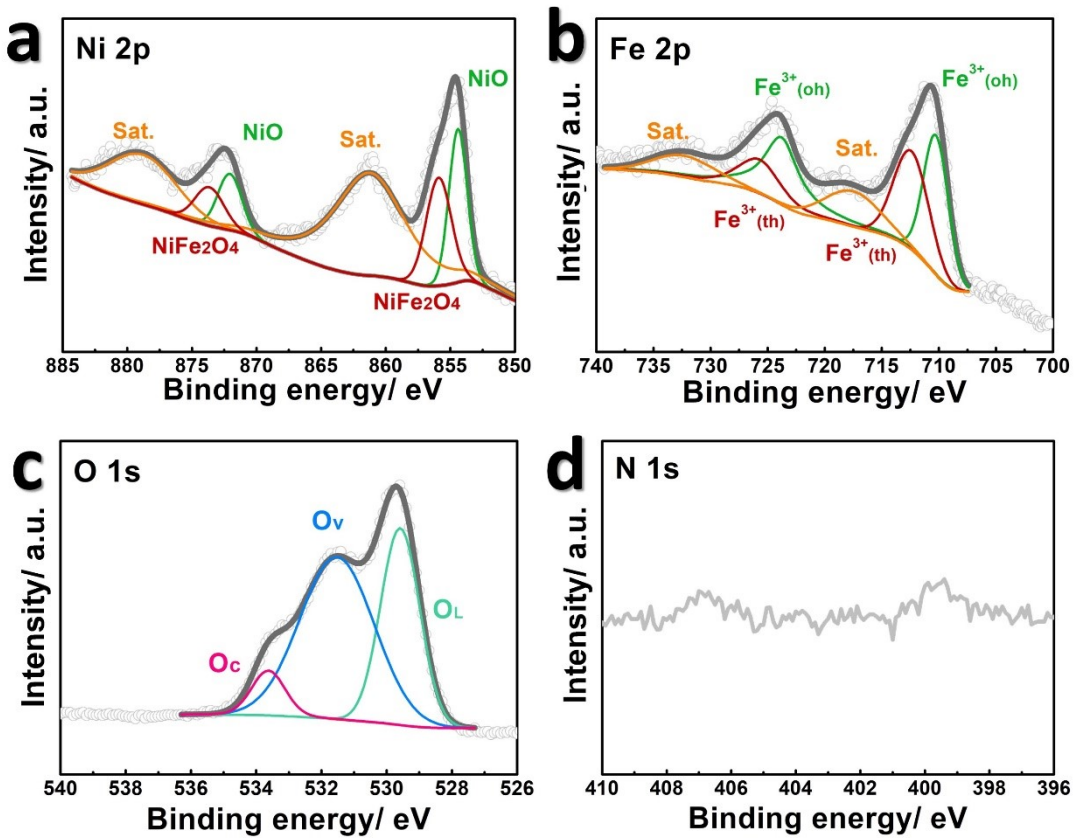

Figure S9. High-resolution XPS spectrum of NiFe-350 : (a) Ni 2p, (b) Fe 2p, (c) O 1s and (d) N 1s.

The splitting peak of 854.4 and 872.6 eV should be attributed to in NiO and peaks at 855.9 and 873.7 eV should be attributed to $NiFe_2O_4$, respectively. The other peaks correspond to the satellite peaks of Ni.[4, 5] The peaks at 710.3 and 723.8 eV are attributed to Fe^{3+}(oh) and peaks at 712.5 and 725.8 eV are attributed to Fe^{3+} (th), respectively. The other peaks correspond to the satellite peaks of Fe.[5] The peaks at 529.7, 531.3 and 533.3 eV are attributed to O_L, O_v and O_c, respectively.[6]

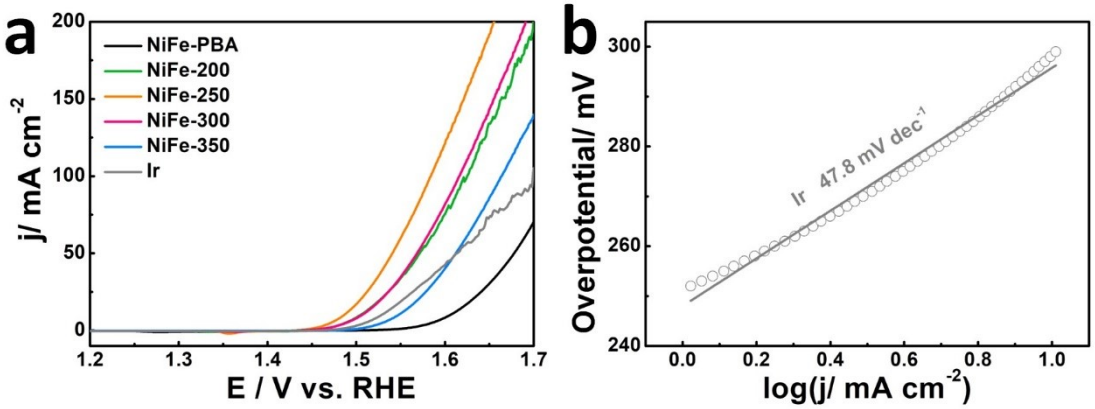

Figure S10. (a) LSV of NiFe-PBA, NiFe-200, NiFe-250, NiFe-300, NiFe-350 and Ir. (b) Tafel slopes of Ir.

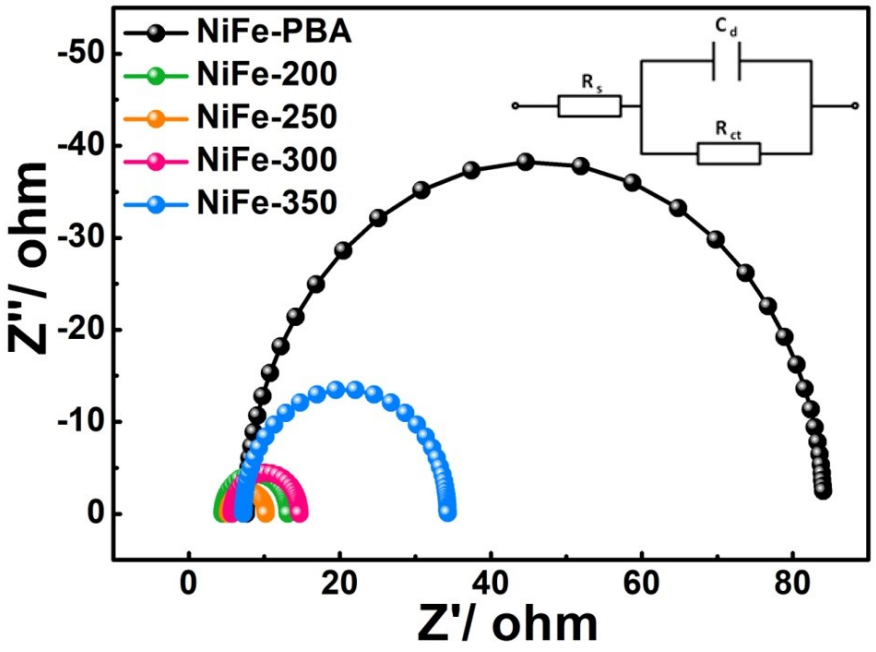

Figure S11. Fitted Nyquist plots of NiFe-PBA, NiFe-200, NiFe-250, NiFe-300, and NiFe-350.

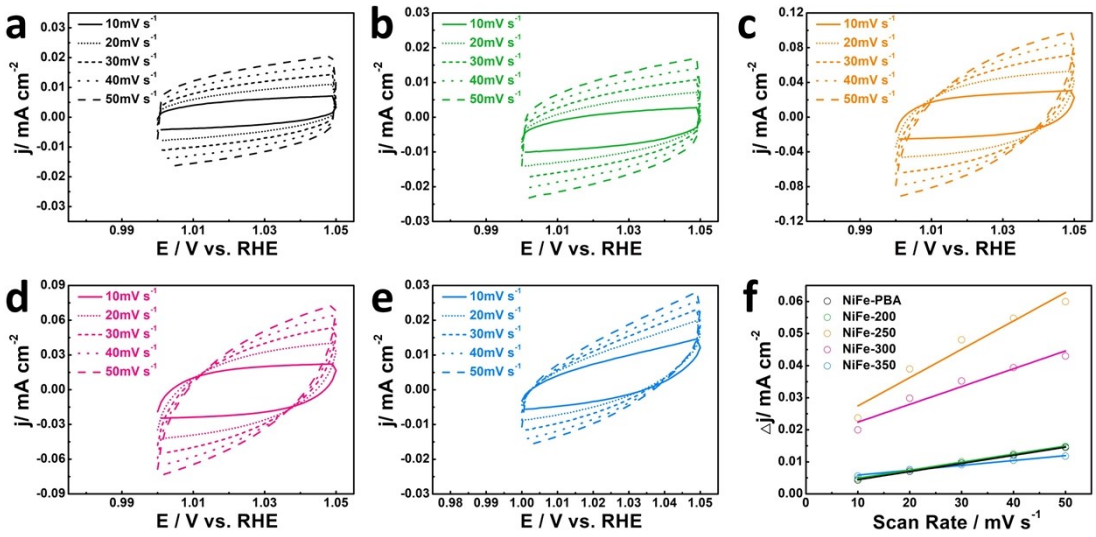

Figure S12. CVs of (a) NiFe-PBA, (b) NiFe-200, (c) NiFe-250, (d) NiFe-300 and (e) NiFe-350 at the different scan rates from 10−50 mV s^{-1} in the potential range of 1.00−1.05 V vs RHE; (f) capacitive current at 1.03V vs. RHE as a function of scan rate for NiFe-PBA, NiFe-200, NiFe-250, NiFe-300 and NiFe-350.

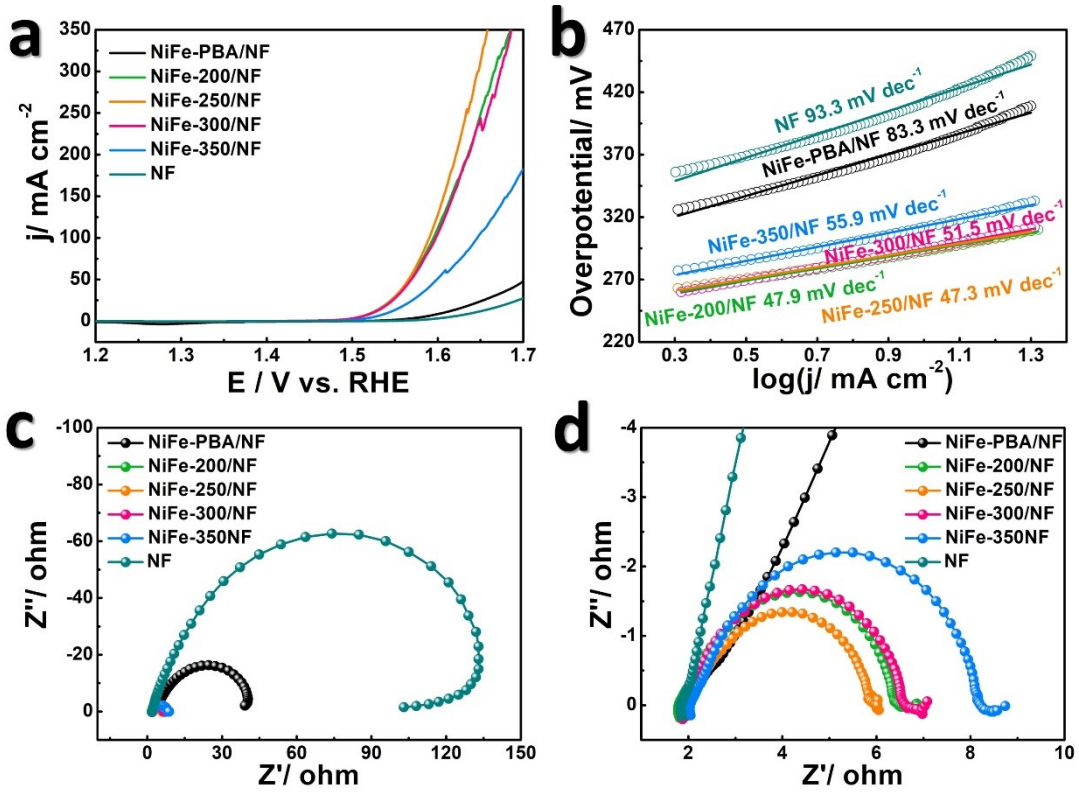

Figure S13. (a) LSV, (b) Tafel slopes, (c) and (d) Nyquist plots of NiFe-PBA/NF, NiFe-200/NF, NiFe-250/NF, NiFe-300/NF and NiFe-350/NF.

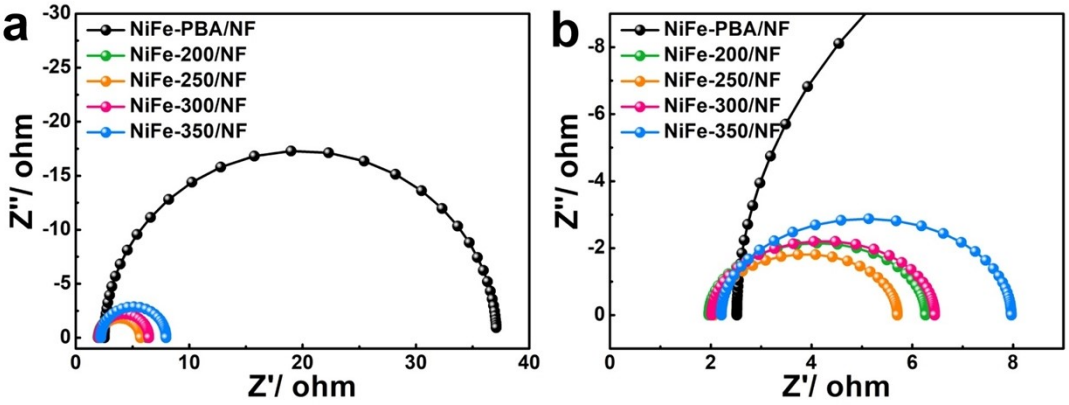

Figure S14. Fitted Nyquist plots of NiFe-PBA/NF, NiFe-200/NF, NiFe-250/NF, NiFe-300/NF, and NiFe-350/NF.

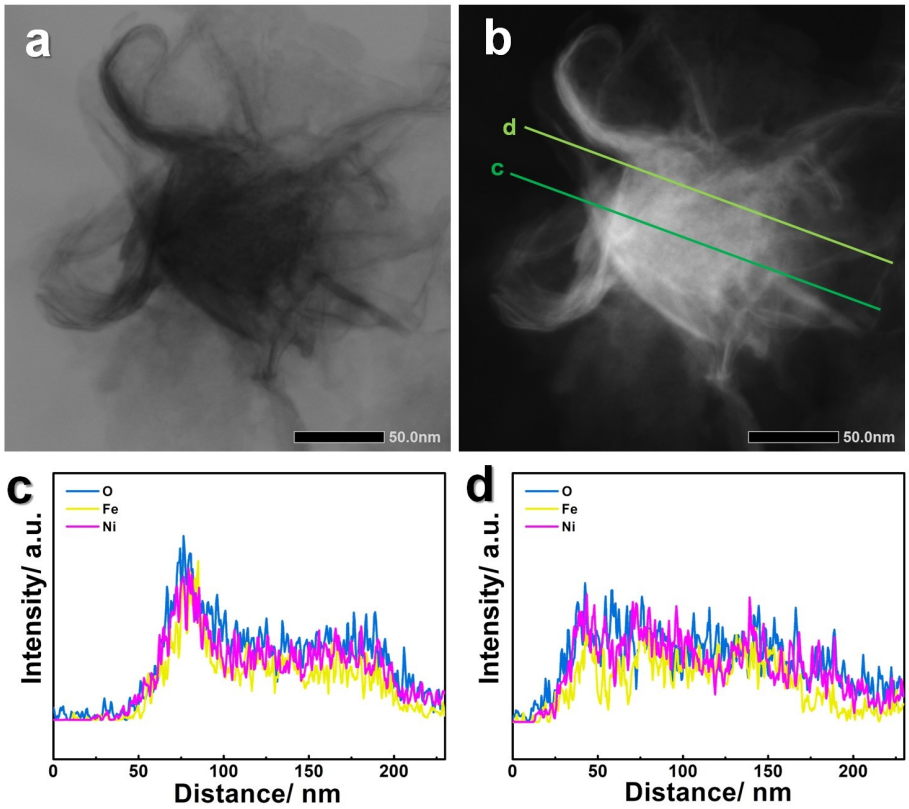

Figure S15. (a) TEM and (b) HAADF-STEM images of NiFe-250-A. Elemental distributions of Ni, Fe and O extracted from HAADF-STEM line profiles across the particle center (c) and edge (d).

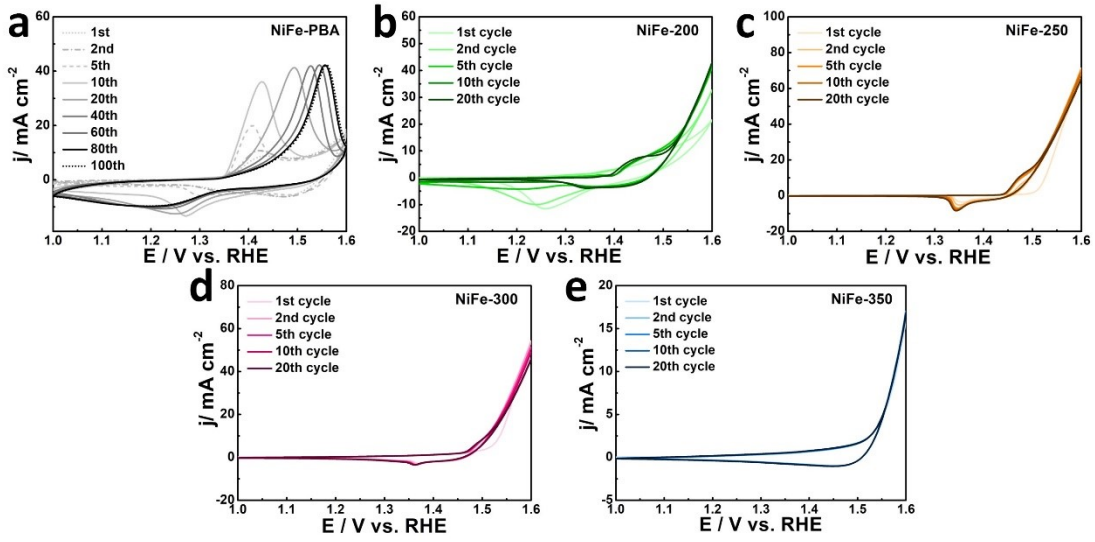

Figure S16. (a) CV curves of NiFe-PBA at a scan rate of 50 mV s^{-1} in 1M KOH for 1st, 2nd, 5th, 10th, 20th, 40th, 60th, 80th and 100th. CV curves of (b) NiFe-200, (c) NiFe-250, (d) NiFe-300 and (e) NiFe-350 at a scan rate of 50 mV s^{-1} in 1M KOH for 1st, 2nd, 5th, 10th, 20th.

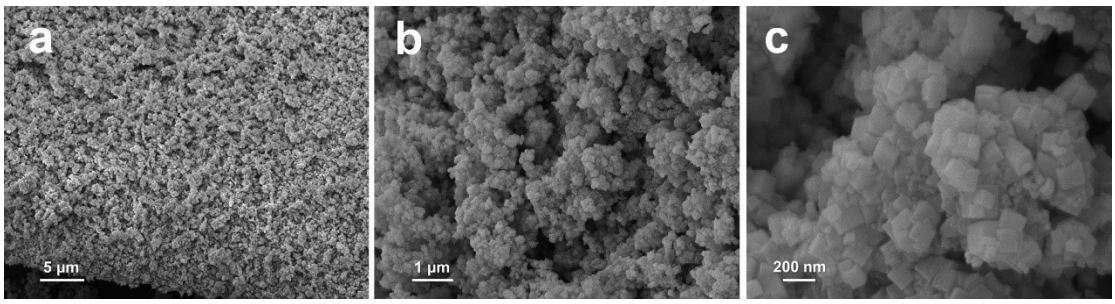

Figure S17. SEM images of NiFe-PBA@NF.

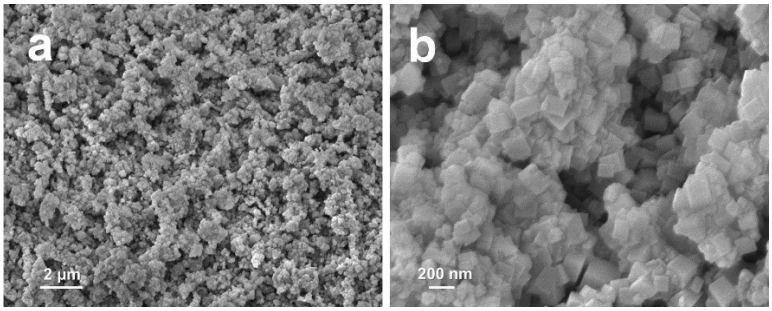

Figure S18. SEM images of NiFe-250@NF.

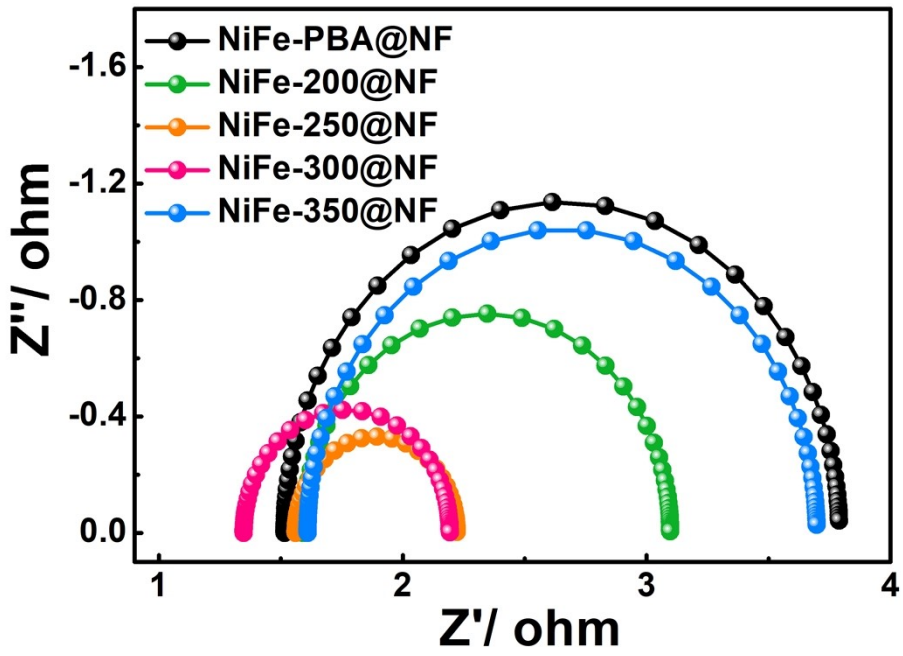

Figure S19. Fitted Nyquist plots of NiFe-PBA@NF, NiFe-200@NF, NiFe-250@NF, NiFe-300@NF, and NiFe-350@NF.

Table S1. Electrochemical impedance analysis of NiFe-PBA, NiFe-200, NiFe-250, NiFe-300, and NiFe-350.

Samples	R_s/Ω	R_{ct}/Ω cm^{-2}
NiFe-PBA	7.584	76.50
NiFe-200	4.491	8.638
NiFe-250	5.206	4.988
NiFe-300	5.713	8.939
NiFe-350	7.249	27.03

Table S2. Electrochemical impedance analysis of NiFe-PBA/NF, NiFe-200/NF, NiFe-250/NF, NiFe-300/NF, and NiFe-350/NF.

Samples	R_s/Ω	R_{ct}/Ω cm^{-2}
NiFe-PBA/NF	2.520	34.59
NiFe-200/NF	1.963	4.303
NiFe-250/NF	2.072	3.633
NiFe-300/NF	2.022	4.423
NiFe-350/NF	2.212	5.754

Table S3. Electrochemical impedance analysis of NiFe-PBA@NF, NiFe-200@NF, NiFe-250@NF, NiFe-300@NF, and NiFe-350@NF.

Samples	R_s/Ω	R_{ct}/Ω cm^{-2}
NiFe-PBA@NF	1.516	2.274
NiFe-200@NF	1.591	1.506
NiFe-250@NF	1.561	0.660
NiFe-300@NF	1.348	0.845
NiFe-350@NF	1.610	2.087

Sample	XPS	EDS	ICP-OES
	Ni/Fe Ratio	Ni/Fe Ratio	Ni/Fe Ratio
NiFe-250	1.16	1.20	1.19
NiFe-250-A	1.25	1.29	1.24

Table S4. Ni/Fe atomic ratios determined by XPS, EDS, and ICP-OES analyses.

Table S5. Comparison of OER activity of recently reported electrocatalysts derived from PBA precursors.

Electrocatalyst	Substrate	Overpotential at X mA cm^{-2} (mV)	Tafel slope (mV dec^{-1})	Ref.
NiFe-250	GC	η_{10}=255	39.4	This
NiFe-250@NF249	NF	η_{10}=230	39.4	work
PBA-3h-A (Air Plasma 3h)	NF	η_{10}=251	62.1	1
NiOOH/FeOOH NBs	GC	η_{10}=220	60.28	2
	NF	η_{10}=216		
PBA-SMo/NF-10	NF	η_{10}≈230 η_{20}=252 η_{100}=294	64	3
Ni@$CoFe_2O_4$-250	NF	η_{10}≈320 η_{100}=415	72.64	6
porous NiCoFe-P-NP@NiCoFe-PBA nanocage	GC	η_{10}=223	78	7
v-NiFe-PBA@rGO	GC	η_{10}=251	36.2	8
Ar-U-CoFe PBA	GC	η_{10}=305	36.1	9
N-doped hollow NiCoPBA/NF	NF	η_{10}=289	70	10
ZnCoHCF-3	GC	η_{10}=350	79	11
Ni-Fe-Se nanocages	CP	η_{10}=249	36	12
O-PBA/N-CNT	NF	η_{10}=280	48	13
CoFeZn-PBA	GC	η_{10}=343 η_{60}=449 η_{100}=511	75	14
O-NiCoP Cages	GC	η_{10}=310	84	15
CoFeP/NF	NF	η_{10}=253 η_{60}=290	36	16
Au@$CoFe^{II}$(thick)	GC	η_{10}=340	63±5	17
	NF	η_{10}=300	48	

GC: Glassy carbon
NF: Ni Foam
CP: Carbon paper

References

1. W.-B. Wang, H.-J. Cao and G.-L. Li, *Inorg. Chem.*, 2023, **62**, 10241-10248.
2. L. Qiu, Q. Wang, P. Yan and X.-Y. Yu, *J. Mater. Chem. A*, 2022, **10**, 21251-21259.
3. C. Zhang, J. Chen, J. Zhang, Y. Luo, Y. Chen, Y. Xue, Y. Yan, Y. Jiao, G. Wang and R. Wang, *J. Colloid Interf. Sci.*, 2022, **607**, 967-977.
4. Z. Cao, T. Zhou, X. Ma, Y. Shen, Q. Deng, W. Zhang and Y. Zhao, *ACS Sustainable Chem. Eng.*, 2020, DOI: 10.1021/acssuschemeng.0c04049.
5. S. Pal, S. Jana, D. K. Singh, V. Ganesan, U. P. Azad and R. Prakash, *Int. J. Hydrogen Energy*, 2024, **50**, 52-65.
6. Y. Hao, G. Du, Y. Fan, L. Jia, D. Han, W. Zhao, Q. Su and B. Xu, *Appl. Surf. Sci.*, 2023, **614**, 156237.
7. G. Zhang, Y. Li, X. Xiao, Y. Shan, Y. Bai, H.-G. Xue, H. Pang, Z. Tian and Q. Xu, *Nano Lett.*, 2021, **21**, 3016-3025.
8. S. Jo, J. Kwon, S. Choi, T. Lu, Y. Byeun, H. Han and T. Song, *Appl. Surf. Sci.*, 2022, **574**, 151620.
9. F. Diao, M. Rykær Kraglund, H. Cao, X. Yan, P. Liu, C. Engelbrekt and X. Xiao, *J. Energy Chem.*, 2023, **78**, 476-486.
10. H. T. Le, J. E. Lee, S. Y. Yun, O. Kwon, J. K. Park and Y. K. Jeong, *Int. J. Mol. Sci.*, 2023, **24**, 9246.
11. P. Jain, S. Jha and P. P. Ingole, *ACS Appl. Energy Mater.*, 2023, **6**, 3278-3290.
12. Z.-P. Wu, H. Zhang, S. Zuo, Y. Wang, S. L. Zhang, J. Zhang, S.-Q. Zang and X. W. Lou, *Adv. Mater.*, 2021, **33**, 2103004.
13. S. Aulia, Y.-C. Lin, L.-Y. Chang, Y.-X. Wang, M.-H. Lin, K.-C. Ho and M.-H. Yeh, *ACS Appl. Energy Mater.*, 2022, **5**, 9801-9810.
14. H. Zou, X. Liu, K. Wang, Y. Duan, C. Wang, B. Zhang, K. Zhou, D. Yu, L.-Y. Gan and X. Zhou, *Chem. Commun.*, 2021, **57**, 8011-8014.
15. D. Li, C. Zhou, Y. Xing, X. Shi, W. Ma, L. Li, D. Jiang and W. Shi, *Chem. Commun.*, 2021, **57**, 8158-8161.
16. D. Xiong, C. Lu, C. Chen, J. Wang, Y. Kong, T. Liu, S. Ying and F.-Y. Yi, *J. Power Sources*, 2022, **520**, 230884.
17. R. Sanchis-Gual, T. F. Otero, M. Coronado-Puchau and E. Coronado, *Nanoscale*, 2021, **13**, 12676-12686.